

See discussions, stats, and author profiles for this publication at: <https://www.researchgate.net/publication/263943258>

Atomistic Modeling of the Electrode–Electrolyte Interface in Li–Ion Energy Storage Systems: Electrolyte Structuring

ARTICLE in THE JOURNAL OF PHYSICAL CHEMISTRY C · FEBRUARY 2013

Impact Factor: 4.77 · DOI: 10.1021/jp3102282

CITATIONS

27

READS

85

4 AUTHORS, INCLUDING:



Revati Kumar

Louisiana State University

23 PUBLICATIONS 599 CITATIONS

SEE PROFILE



Daniel P. Abraham

Argonne National Laboratory

148 PUBLICATIONS 3,257 CITATIONS

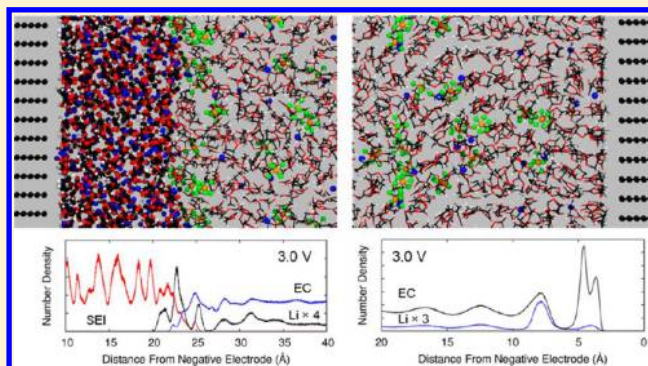
SEE PROFILE

Atomistic Modeling of the Electrode–Electrolyte Interface in Li-Ion Energy Storage Systems: Electrolyte Structuring

Ryan Jorn,^{†,‡} Revati Kumar,^{†,§} Daniel P. Abraham,^{||} and Gregory A. Voth^{*,‡,§,⊥}[†]Computing, Environment, and Life Sciences Division, Argonne National Laboratory, 9700 South Cass Avenue, Argonne, Illinois 60439, United States[§]Department of Chemistry, University of Chicago, 5735 South Ellis Avenue, Chicago, Illinois 60637, United States^{||}Chemical Sciences and Engineering Division, Argonne National Laboratory, 9700 South Cass Avenue, Argonne, Illinois 60439, United States[⊥]James Franck Institute, Institute for Biophysical Dynamics, and Computation Institute, University of Chicago, 5735 South Ellis Avenue, Chicago, Illinois 60637, United States

S Supporting Information

ABSTRACT: The solid electrolyte interface (SEI) forms as a result of side reactions between the electrolyte and electrode surfaces in Li-ion batteries and can adversely impact performance by impeding Li-ion transport and diminishing the storage capacity of the battery. To gain a detailed understanding of the impact of the SEI on electrolyte structure, atomistic molecular dynamics simulations of the electrode/electrolyte interface were performed in the presence and absence of the SEI under applied voltages. The composition of the SEI was guided by a wealth of data from experiments and allowed to vary across the simulations. A novel computational approach was implemented that showed significant computational speedup compared to fully polarizable electrode simulations, yet, retained the correct qualitative physics for the electrolyte. A force-matching algorithm was used to construct a new force field for the pure electrolyte, LiPF₆ in ethylene carbonate, which was developed from ab initio molecular dynamics simulations. The electrode/electrolyte interface was included using a simple, physically motivated model, which includes the polarization of the conducting graphitic electrode by the electrolyte and the application of an external voltage. Changes in the structure of the electrolyte at the interface as a function of applied voltage, the thickness of the SEI layer, and composition of the SEI provide molecular level insight into the species present at these interfaces and potential clues to the effect of the SEI on transport. It is noted that, with increasing SEI thickness and LiF content, lithium ions are drawn closer to the SEI surface, which implies that these interfaces favor desolvation and promote more rapid lithium transport.



1. INTRODUCTION

While lithium ion batteries have fueled a revolution in personal electronics, their impact on the automotive industry has yet to achieve similar success. The delay arises in part from the contrast between the energy and power demands for hand-held devices, such as laptop computers and cell phones, with the need for quick acceleration and sustained driving ranges in electrified vehicles to make them competitive with internal combustion engines.^{1,2} There is ample motivation to pursue alternative energy sources for the transportation sector, in particular, because it is responsible for a substantial portion of the green house gas emissions and, hence, implicated in global climate change.^{3,4} The role of electrochemical energy storage is also not limited to automotives. The intermittence of several “green energy” technologies, such as solar and wind power, emphasize the need to improve stationary energy storage to

distribute power to the grid when the sun is not visible and when there is no breeze to drive the wind turbines.⁵

Improving battery performance is a highly coupled process between the electrodes and the electrolyte that is further complicated by the presence of reactive interfaces between the two resulting in electrolyte breakdown.^{6–8} The gradual decomposition of the solvent and salt at the electrode interface reduces the overall lifetime of the battery by trapping the active component, lithium ions, in surface films and also degrades the rate of discharge available to power an external circuit. Fortunately, decomposition of the electrolyte to form solid surface films passivates the electrode against further reactions with the electrolyte and allows lithium ion conduction. This

Received: October 16, 2012

Revised: January 13, 2013

Published: January 25, 2013

combination of favorable ion conduction with minimal electron transport has led to the term solid electrolyte interphase (SEI) to describe the layer of electrolyte breakdown products formed during lithium ion battery charge cycling.⁹ SEIs have been reported to form on a variety of electrode surfaces; however, the reactions at carbon material interfaces with cyclic carbonate-based electrolytes are some of the most intensely studied as a result of their commercial prevalence.^{6,8,10} The thickness of the films formed on graphite particles depends on the duration of battery operation¹¹ and generally range from nanometers to tens of nanometers.^{12,13} A number of parameters are known to influence the composition of graphitic SEIs,⁷ including selection of solvent and salt for the electrolyte,^{14,15} the type of graphitic carbon used in the cell,¹⁶ the preparation of the carbon anode,¹⁷ the nature of the graphite planes exposed to the electrolyte,^{13,15,18} and the temperature of the system.¹⁹ Common species attributed to the decomposition of standard ethylene carbonate and linear carbonate electrolytes include organic species such as dilithium ethylenedicarbonate (Li_2EDC) and various lithiated alkoxides, as well as inorganics such as lithium carbonate, lithium fluoride (arising from salt decomposition), and lithium oxide.^{7,20–25}

Aside from the composition of the surface films, their structures remain highly debated.⁸ One important question remains: the role of solvent cointercalation with lithium as it enters the gap between graphite edge planes.²⁶ While cointercalation of solvent molecules with lithium is attributed to the destructive exfoliation of graphite particles in propylene carbonate (PC), the extent of solvent insertion with other species is unclear and could form a competing process with direct decomposition on the surface.^{27,28} As has been pointed out previously,⁶ a second complication to understanding SEI structure stems from the interpretation of experimental results. The ex situ nature of several foundational experiments on the structure and composition of the SEI could have suffered from decomposition of the native organic species as a result of interaction with atmospheric contaminants.²¹ Nevertheless, a commonly accepted model for the SEI¹³ suggests a layer of dense inorganic compounds at the electrode interface with a conversion to predominantly organic compounds near the solvent-exposed side. While atomic level resolution of the SEI structure is still lacking, it is anticipated that the continual development of in situ techniques^{20,22,24,28,29} may provide additional insights into the often opposing reports in the literature.

Because the solid electrolyte interphase provides a major bottleneck to lithium transport, having a deeper understanding of the composition and structure of the SEI is critical to developing guidelines for optimizing the rate performance of battery cycling.³⁰ Electrochemical impedance spectroscopy (EIS) has been used with phenomenological equivalent circuit fitting to estimate the activation energies for both lithium ion desolvation at the electrode–electrolyte interface as well as lithium insertion into the SEI.^{25,30–33} The activation energies obtained indicate that the process of desolvation is the rate determining step for lithium ion conduction, but was seen to vary between different electrodes, even as the composition of the electrolyte remained unchanged.³³ Additional experiments with controlled compositions of the electrolyte and known compositions in the SEI²⁵ introduced the possibility to develop composition–function relationships for the surface films. By understanding which components favor rapid lithium insertion and diffusion, guidelines could eventually be developed for

improved interfaces. A clear understanding of the connections between composition, structure, and ion transport characteristics has been severely lacking for the electrode–SEI–electrolyte interface⁸ and forms the motivation for the work presented in this manuscript.

Given the complications present in the experimental characterization techniques, it is anticipated that a close synergy between experiments and atomistic computational modeling can play a significant role in advancing our understanding of the relationships between interface structure and transport properties.³⁴ To date, efforts to model the SEI from an atomistic perspective have largely focused on reaction mechanisms. The oxidation and reduction of common carbonate solvents have been investigated for over a decade.^{35–39} These studies have recently emphasized the influence of counterions and the solvent molecules in the first solvation shell, and beyond, on the reaction path.^{40–42} The mechanism for EC reduction suggested by these studies, in combination with results from experiment,¹⁰ involves two limits in concentration. When there is a high concentration of EC at the electrode interface, a one-electron reduction pathway is favored of which Li_2EDC is a major product. For sufficiently low concentrations of EC, however, there is a tendency toward a two-electron reaction that favors Li_2CO_3 . Standard quantum chemistry calculations based on transition state searches were recently extended by parametrization of a reactive force field simulation, capable of explicitly accounting for the surrounding electrolyte, beyond typical polarizable continuum models, and granting access to longer time scales than feasible with ab initio techniques.⁴³ At sufficiently high EC density, qualitative agreement with the above mechanism was seen in these ReaxFF simulations with Li_2EDC being a predominant product.

Ab initio calculations focusing on the behavior of reactants in bulk liquids overlook critical aspects of the physics of electrochemical systems: for example, the effect of the electrode surface and applied electric fields on local electrolyte structuring at the interface. Early molecular dynamics (MD) simulations attempted to study transport at the clean graphite–electrolyte interface, without an SEI present, but these studies were very limited in sampling size.⁴⁴ More extensive work was performed later by Smith and co-workers for a variety of electrode surfaces ranging from lithiated iron phosphate to the basal and edge planes of graphite.^{45–47} Their focus was on the differential capacitance of the double layers formed at these interfaces and their studies form an important benchmark for method development. Their method was based on the careful construction of force fields from ab initio data, explicitly accounting for atomic polarizabilities, and self-consistent charging of the electrode surfaces to produce a target bias potential. While the application of oscillating electric fields has also been considered within MD,⁴⁸ our attention will be restricted to constant voltage molecular dynamics simulations with comparison to AC experiments left for future work.

Previous modeling which accounted for SEI components on explicit graphite surfaces largely focused on Li_2EDC in limiting scenarios and modeled the growth of SEI films with reactive methods. Regarding the former, the adsorption energy and film cohesion of Li_2EDC were studied at graphite surfaces in the gas phase and, hence, excluded the presence of the organic electrolyte.^{37,49} While appropriate to the description of processes taking place deeper within the electrode,⁵⁰ such studies provide no information pertaining to structure at the in situ SEI–electrolyte interface. Related work by Tasaki and

Harris investigated the solubility of SEI components in various organic solvents by considering the dissolution of single molecules in a periodic box of EC and DMC,⁵¹ but in this case the presence of the electrode surface was not considered. Ambitious reactive methodologies have been reported that attempt to account for all three phases, that is, electrode–SEI–electrolyte, with *ab initio* molecular dynamics (AIMD) simulations^{41,52,53} and reactive force fields.⁵⁴ These studies are aimed at probing the reactions at the electrode interfaces on two disparate time scales: initiation of the SEI on the order of picoseconds and propagation of the SEI on the time scale of nanoseconds. While encouraging agreement was seen with experiments regarding the reaction products, the AIMD simulations are very computationally expensive and prohibitive to studying SEI growth on the scale of experiments. On the other hand, by allowing for free evolution of the reactants, AIMD is an important complement to standard transition state searches for reactions. The reactive classical molecular dynamics model developed by Kim et al. using a parametrized force field (ReaxFF)⁵⁴ allows for investigating SEI growth at the nanometer scale with few restrictions on the chemistry allowed to take place at lithium metal and graphite surfaces. They reported substantial gas evolution in the system, possibly explaining the reported porous nature of the SEI and the development of a layered system in agreement with the common model for the graphitic SEI (inorganic components at the electrode surface and organic components at the electrolyte interface).

Investigation of the lithium ion transport in the solid electrolyte interphase with computational modeling has focused on simple cases for the materials involved at the atomistic level and efforts to account for the resistance of the SEI in mass transport calculations from the vantage point of whole cell engineering. Efficient pathways for the transport of excess interstitial lithium and lithium vacancies through lithium carbonate crystals have been identified using a combination of DFT and nudged elastic band methods.^{55,56} These studies were extended to other SEI species including lithium oxide and lithium fluoride, which showed that lithium fluoride had the highest barriers to lithium transport and lithium oxide the smallest barriers.⁵⁵ While both cases are too idealized to compare with the complex structures seen in SEI experiments, they provide an important starting point for further work. In contrast to studies on crystalline materials, the diffusive behavior of Li in amorphous Li₂EDC was also reported, and the diffusion mechanism was shown to rely on a percolating-type network of lithium sites exchanging ions on a time scale faster than the relaxation of the EDC²⁻ groups.⁵⁷ Continuum-based models have been foundational to understanding the complex array of mass transport phenomena at cathode– and anode–electrolyte interfaces^{58–64} and the general impacts of SEI formation on battery performance,^{65–67} however, they lack a clear connection to atomistic information and often rely on a macrohomogeneous approximation in combination with empirical fitting. The latter requirements limit predictive capability for developing new materials and interfaces but provide an important rationalization for experimental observations.

Taken together, the previous atomistic work on battery systems has largely focused on SEI formation, but the properties of the electrode–SEI–electrolyte interface have received little attention. Given the rate determining behavior of the SEI–electrolyte interface, further atomistic studies are well

motivated with the goal of providing guidance to continued experimental efforts to improve battery design. In this work we report the first simulations to our knowledge of the SEI–electrolyte interface for lithium ion rechargeable batteries in the presence of applied fields. Our choice of system is experimentally justified and our selection of SEI components is based on both the available experimental data and a desire to understand the effect of the SEI on electrolyte structuring using a minimal model. In section 2, we describe the method used to probe these interfaces which arises from a novel combination of an empirical MD model force-matched from *ab initio* MD for the LiPF₆ in the electrolyte, the incorporation of a force field for the SEI materials Li₂EDC and LiF, and the introduction of a recently developed computationally efficient image charge method to account for electrode polarization and applied potential. In section 3, we compare our results to previous work on bare graphite surfaces and find excellent agreement, indicating that our computationally efficient method is suitable to apply to these interfaces. Subsequently, we apply the same machinery to graphite interfaces with the presence of an SEI built from Li₂EDC and LiF of varying thickness and composition. The Poisson potentials for these systems are compared and the density profiles of each species present are discussed with respect to the SEI parameters of thickness and percent LiF in the composition. Finally, we conclude with the implications of the structural information obtained and describe extensions of this work currently underway to probe the impact of these interfaces on lithium transport.

2. METHODS AND COMPUTATION

2.1. Force Field Development. The composition of the electrolyte was chosen for simplicity and experimental relevance to be ethylene carbonate (EC) with LiPF₆ dissolved at 1 M concentration. This pairing, along with the related salt LiBF₄, has been studied previously with AIMD⁶⁸ and classical MD based on pairwise force fields^{69–73} and polarizable models.^{44,74} The COMPASS⁷⁵ force field, along with its predecessors CFF91 and CFF93,^{76,77} has been used extensively for EC-based electrolytes and relies on a complex set of interactions between bonds, angles, dihedrals, and out-of-plane motions. Tasaki et al. have implemented this force field in combination with charge fitting to electronic structure potentials to study solvation properties and obtained reasonable agreement for heats of vaporization for pure EC.^{37,51} COMPASS has the benefit of being developed based on electronic structure calculations, tailored to agree with thermal properties of various materials, and having been trained on a wide variety of chemical groups as a general purpose force field, including a significant emphasis on carbonates in its lineage.^{70,77} Interestingly, Masia et al. showed that fitting bonding and angle interactions to general polynomials elucidates the importance of the anharmonic terms included in the COMPASS force field to correctly account for the vibrational spectrum of EC.⁷² However, force fields which rely on strictly pairwise intermolecular interactions also appear to overstructure ethylene carbonate around the lithium ions in comparison with polarizable models and AIMD.^{68,74} The polarizable model of Borodin and Smith,⁷⁴ developed by detailed fitting to quantum chemistry calculations, demonstrated more favorable agreement with the limited experimental data on radial distribution functions for cyclic carbonate electrolytes and showed agreement for a variety of experimentally determined thermal and transport properties.

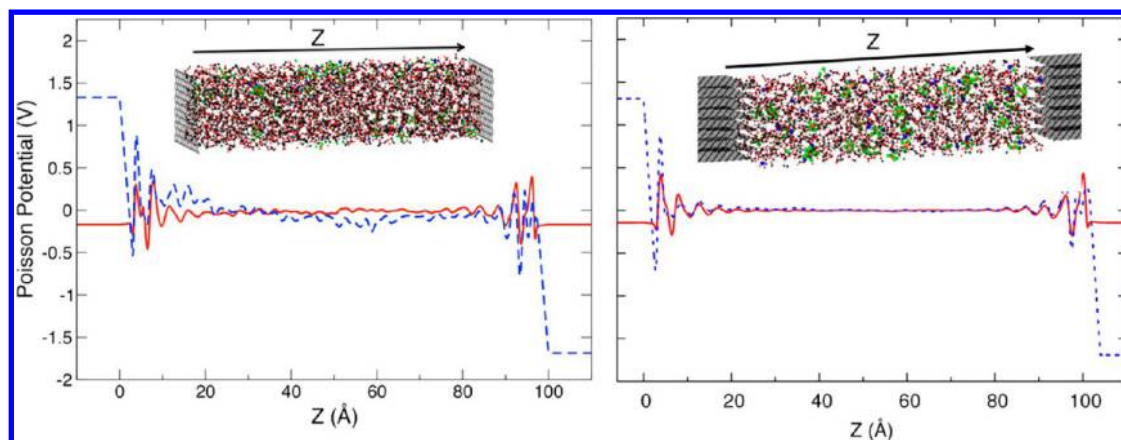


Figure 1. Example of poisson potentials across the electrochemical simulation cell without an SEI present at applied potentials at 0 V (red lines) and 3 V (blue dotted lines). In the left panel, the basal plane electrodes are shown with the resulting potential function, while in the right panel the electrode with edge planes exposed to the electrolyte is shown with corresponding potentials. Distance from the left electrode is denoted as Z , and the carbons atoms are shown in black, hydrogen in white, oxygen in red, lithium in blue, phosphorus in orange, and fluorine in green.

A potential disadvantage in their approach is the higher computational cost associated with such simulations accounting for molecular response to local electrostatic fields and raises the question of whether a better balance can be obtained between accuracy and speed of computation in modeling battery electrolytes.

One goal in this work is to apply a particular implementation of the force-matching algorithm^{78–80} to nonaqueous electrolytes to better capture the solvation structure of lithium ions while maintaining a simpler representation for the force field. In the absence of the SEI, the constituents of the electrochemical cell are the Li^+ cation, the PF_6^- anion and the ethylene carbonate (solvent). Fortunately, accurate nonpolarizable models for single ethylene carbonate molecules exist in the literature and form a useful basis upon which to build our model. The force field chosen for the ethylene carbonate solvent is based on the work by Masia et al.,⁷² while the partial charges for the intermolecular interactions were determined from an electrostatic potential study of the monomer from DFT. The Lennard-Jones (LJ) parameters were taken from Carlson and co-workers.⁸¹

A brief description of our force-matching algorithm is provided here for completeness and the interested reader is referred to the extensive literature on the topic for further details.^{78–80,82,83} A periodic box of EC molecules, with Li^+ and PF_6^- added to yield the correct concentration, was simulated using ab initio molecular dynamics (AIMD). Configurations were chosen at random from these trajectories and the forces on the nuclei fitted to a host of parameters from a model force field until the forces from the model match the ab initio forces. In other words, a least-squares fit is performed so as to minimize the variational residual, χ^2 , which is given by

$$\chi^2 = \frac{1}{N} \left\langle \sum_{i=1}^N (\vec{f}_i^{\text{ab}} - \vec{f}_i^{\text{ff}})^2 \right\rangle \quad (1)$$

where \vec{f}_i^{ab} is the ab initio force on particle i and \vec{f}_i^{ff} is the corresponding force from the model potential. In this case, only the forces on the Li^+ cation and the atoms of the PF_6^- anion were used in the above equation. The partial charges on the anion were determined using the Merz–Kollmann⁸⁴ electrostatic fitting method and only the Lennard-Jones parameters of

the ions and its intramolecular force constants were determined using the force-matching algorithm.

The AIMD simulation was carried out with the CP2K^{85,86} code using the PBE functional and the TZ2VP basis set, with pseudopotentials to represent the core electrons. The system consisted of 28 ethylene carbonates and 2 Li^+ and 2 PF_6^- ions in a cubic simulation box of length 15.24 Å, corresponding to a 1 M solution of LiPF_6 , with periodic boundary conditions at a temperature of 300 K. The initial configuration was obtained from a 100 ps constant NVT simulation of the system with the AMBER force field using the LAMMPS software package.^{87,88} The resulting configuration was equilibrated with AIMD for 10 ps at 300 K after which a production run of 30 ps was carried out in the constant NVE ensemble. The partial charges on the atoms of the PF_6^- ion were obtained using the Merz–Kollmann ESP method on the monomer with the TZVP basis set and the PBE functional. The GAUSSIAN09⁸⁹ suite of programs was used to perform this calculation.

The force field obtained from the force-matching code was used subsequently to simulate a 1 M solution of LiPF_6 in ethylene carbonate at a temperature of 300 K using LAMMPS. The simulation box consisted of 201 ethylene carbonate molecules with 15 Li^+ and PF_6^- ions in a cubic box of length 29.44 Å. The system was equilibrated for 3 ns after which a production run was carried out in the constant NVE ensemble for 6 ns.

While extensive work was invested into a new force field for the electrolyte, the solid electrolyte interphase materials were instead described by the standard CFF91 model implemented in LAMMPS. Experiments have consistently emphasized the importance of dilithium ethylenedicarbonate in the SEI formed with EC-based electrolytes,^{22,25} and hence, Li_2EDC was chosen for our studies as the dominant component. While the various bonding, angle, torsional, and cross terms were taken from CFF91, the partial charges were calculated using the RESP package in CP2K with the PBE functional in DFT and an all-electron 6-311G** basis set. In addition to this organic component, a frequently reported inorganic species in the SEI film arises from the breakdown of the salt anion PF_6^- to form LiF .^{7,10} Without a precise estimate for the amount of salt reaction product present in the interphase, simulations were performed including varying mass ratios for LiF embedded in Li_2EDC . While the partial charges for LiF were directly

obtained, the Lennard-Jones parameters were taken from crystal parameters obtained with the CFF93 force field.⁹⁰ The standard mixing rules for the CFF Lennard-Jones parameters were implemented and the P3M method was used to incorporate long-range electrostatics. Extensive simulations were conducted on the bulk solid phase properties of interphase materials comprised of varying ratios of Li₂EDC and LiF to validate our choice of force field (see Supporting Information). Excellent agreement was seen with previous reports using polarizable models for the density and the radial distribution functions of pure Li₂EDC, which provide confidence in our model.

2.2. Model for an In Situ Battery Interface Held at a Constant Potential. A computationally efficient yet accurate atomistic model that captures the essential physics of the electrode interface, namely, the polarization of the electrode by the electrolyte and the imposition of a constant potential difference across the cell was recently developed by Petersen et al.⁹¹ A brief description of the salient features of the model is presented here. The starting point is a cell with two electrodes separated by an electrolyte, shown in Figure 1, in which each electrode has a surface area A and they are separated from each other by a distance D . For every real charge, q_i , in the electrolyte, there will likewise be an induced surface charge on the electrodes, which are assumed to be conductors in the present discussion. By the method of images, it can be shown that the potential experienced by the original charge q_i in the solution can be represented by replacing the conducting surface with an image charge, $-q_i$, located within the electrode. The image charge is located at the same distance from the electrode surface as the real charge in the electrolyte, but reflected onto the other side of the original electrode boundary, also referred to as the image plane. Image charges introduced to account for this initial polarization are referred to as primary image charges. Similarly, each of the induced surface charges on a given electrode will also induce changes in charge density at the other electrode and vice versa. Thus, we have to account for both the primary image charges as well as higher order effects caused by a finite simulation box size. If distances are measured relative to the left electrodes in Figure 1, it can be shown that the sum of these higher order polarizations in each electrode is given by

$$q_{\text{LE}} = \sum_{i=1}^n \frac{q_i z_i}{D}, \quad q_{\text{RE}} = \sum_{i=1}^n \frac{q_i (D - z_i)}{D} \quad (2)$$

where q_{LE} refers to the total induced charge on the left electrode from higher order polarizations, q_{RE} refers to polarization of the right electrode by higher order images, and the index i runs over every charge, q_i , in the electrolyte at a distance z_i from the left electrode surface. If a potential difference V is applied across the cell, then the expressions for the higher order image charges are modified to yield

$$q_{\text{LE}} = \sum_{i=1}^n \frac{q_i z_i}{D} + Q_0, \quad q_{\text{RE}} = \sum_{i=1}^n \frac{q_i (D - z_i)}{D} - Q_0 \quad (3)$$

where the applied voltage is related to the excess charge via $Q_0 = ((V\varepsilon_0 A)/D)$. A useful check on this method is to calculate the Poisson potential from an equilibrated simulation cell with different applied voltages and show that the potential difference across the cell matches the applied voltage. The Poisson potential (Φ) is easily determined from the equilibrium

distribution of the charge density, $\rho(z)$, by integrating Poisson's equation:

$$\nabla^2 \Phi = -\frac{\rho(z)}{\varepsilon_0} \quad (4)$$

To carry out the simulations of the electrolytes in the presence of electrodes and an applied voltage, a modified version of the LAMMPS code, which contains the previously described image charge model, was utilized. Independent DFT calculations have shown that while graphite is by no means a perfect conductor, its response to external fields demonstrates the relevance of this approximation.⁹² Both the basal and edge planes of graphite are considered in the case of pure electrolyte, that is, no SEI layer present, and the representative basal planes of graphite forming two electrodes (see Figure 1) have an interelectrode spacing of 100 Å. The intervening electrolyte consists of 680 ethylene carbonates and 44 Li⁺ and PF₆[−] ions to create a 1 M solution. The simulation is periodic only in the directions parallel to the basal plane, with box lengths of 29.5 and 25.2 Å, respectively, and is not periodic in the direction perpendicular to the surface of the electrodes. For simulations with the edge plane (see Figure 1), the edges of the two electrodes are separated by 104 Å and the simulation box consists of 540 ethylene carbonates and 40 Li⁺ and 40 PF₆[−] ions with box lengths of 26.7 and 25.5 Å in the directions perpendicular to the edge planes. The lack of three-dimensional periodicity was accounted for within the electrostatics calculation in LAMMPS by extending the effective volume of the simulation cell and correcting for dipole interactions between its periodic images.⁸⁸ For both sets of simulations, without an SEI present, equilibration runs of 3 ns at 450 K were carried out, followed by production runs of 5 ns with longer production simulations of 20 ns for the edge planes to ensure statistical convergence. For both the basal plane and the edge plane simulations, applied voltages of 0 and 3 V were considered, in agreement with typical applied fields during battery charge cycling (1.5 V at either end of the simulation cell). Additional simulations at 6 and 7 V were carried out for the basal plane, while for the edge plane, an additional simulation at 4 V was carried out for reasons discussed subsequently in section 3.

To incorporate the SEI films into the simulation, a relatively simple method was adopted following a surface film model which neglects the effects of cointercalation.²⁶ Even in the event of substantial cointercalation, results for the distributions of species at the interface between the SEI and the electrolyte at sufficient SEI thickness should remain relevant. This is because the impact of the cointercalation will be most pronounced directly at the electrode–surface film interface, provided it does not result in significant destruction of the graphite particle, and will be less relevant to the direct electrolyte interface. The simulation cells from the pure electrolyte simulations were modified by insertion of a randomly generated layer of SEI material of varying thickness and composition ranging from 0.5 to 2.0 nm and 0 to 50% by wt LiF. These films were generated to have a slightly higher density than their bulk values, 107% in all cases, in order to ensure good contact with both the electrolyte and electrode region. The electrostatic interactions between the SEI atoms and the electrolyte were given by their partial charges; however, their Lennard-Jones interactions were derived by mapping the electrolyte species into CFF91 force field types and applying the appropriate mixing rules for the

parameters. The equilibration process for each simulation cell after insertion of the random SEI structures involved a 250 ps equilibration with the electrode and electrolyte atoms frozen and a Langevin thermostat set to 453 K. Subsequently, the electrolyte was allowed to move for an additional 250 ps with the image charge interactions turned on and a Nosé-Hoover thermostat set to 450 K. The entire cell, with the exception of the graphite carbon, which remained fixed, was then allowed to relax for an additional 12 ns for each SEI layer considered with a Nosé-Hoover thermostat to simulate the constant NVT ensemble. In general, the presence of the SEI layers required longer equilibration times as a result of the greater disorder at the interfaces and slight compression of the viscous electrolyte. Following the 12 ns equilibration simulation, an additional 12 ns of production data were obtained to study the distribution of EC and ions at the electrolyte–SEI interface. Two challenges present in these simulations are the highly viscous nature of the confined liquid electrolyte, which requires longer simulation times to converge results for the species densities, and the interaction between the image charges and SEI components. Regarding the latter, rare fluctuations of Li^+ ions near the graphite image plane in the SEI resulted in simulation failure from polarization catastrophe as the ions overcame Lennard-Jones barriers to fall into the coulomb well with their image charge. To avoid these rare events, reflective walls were placed at 1.5 Å from the image plane to prevent unphysical lithium insertion. Regarding the statistical sampling in the system, comparison of EC density profiles from 4 to 10 ns windows during the production runs suggested that these results are statistically converged by 6–8 ns; however, the results for the ion distributions suffer from much less sampling in comparison and vary from system to system in their degree of convergence. Given that our present focus is on qualitative comparisons as a function of SEI parameters, observables such as integrated densities of ions were chosen instead of density profiles, which suffered from sampling limitations in some cases.

3. RESULTS AND DISCUSSION

3.1. Bulk Electrolyte and SEI Material Properties. Prior to discussing the complete model for the electrochemical interface, our methods are validated by comparison with previous results for bulk electrolyte properties. Table 1 provides the Lennard-Jones (LJ) parameters from the force-matching algorithm for the intermolecular interactions regarding the PF_6^- anion and Li^+ cation. The charges for the anion were determined using the Merz–Kollmann ESP method and a Lennard-Jones function was used to account for additional

intermolecular forces. During the AIMD for the force-matching procedure, the intramolecular F–P–F angle was set to 90° and the P–F bond length to 1.635 Å based on previous ab initio calculations. A total of 100 configurations were randomly chosen from the AIMD simulation trajectory for use in the force-matching procedure. Simple Lennard-Jones forms for nonbonding interactions, especially in the case of the P atom buried within the fluorine framework, may not be the optimal choice for representing complex AIMD interactions. However, their implementation provides surprisingly good agreement with results from more sophisticated polarizable potentials, as discussed below. Figure 2 shows the excellent agreement

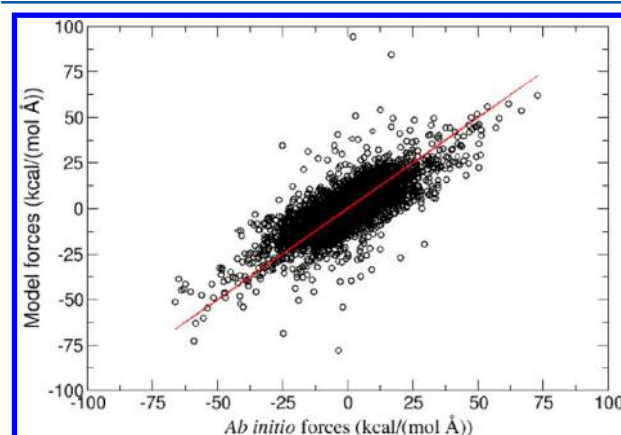


Figure 2. Comparison of the atomic forces on the ions (kcal/(mol Å)) from the ab initio calculations and the force-matched model. Forces from a hundred configurations are compared between the AIMD simulation and the resulting force field. The red line with unit slope is included for reference to the ideal case of a perfect description.

between our force-matched model and the ab initio forces on the atomic sites of the Li^+ and PF_6^- ions, providing further credibility to the choice of interaction function.

A classical molecular dynamics simulation was carried out for a 1 M LiPF_6 solution in ethylene carbonate using the new force-matched model and several radial distribution functions are shown in Figure 3. In the case of the Li–Oc distribution, where the density of carbonyl oxygens from EC (Oc) are shown as a function of distance from lithium ions, a direct comparison is provided between the AIMD and classical MD results. The AIMD peak position and height match the values from previous works using the PBE functional^{53,93} and are comparable to results obtained from neutron scattering experiments.⁹⁴ The polarizable model of Borodin et al. gives the first peak near 2 Å a height of 30, which is close to the AIMD result.⁷⁴ However, the peak heights from other nonpolarizable models in the literature are much higher, in the range of 55–80, contributing to a potential over structuring of the EC, as mentioned earlier.^{70,71} A recent nonpolarizable model developed by Postupna et al. shows an especially high coordination of around 5–6 molecules around the Li^+ ion as opposed to a coordination number of around 4 based on AIMD simulations.⁶⁹ Our results are encouraging, as they suggest that, by using our force-matching procedure, a significantly computationally cheaper model can be obtained that nevertheless shows reasonably good agreement with polarizable methods and experiment, despite the lack of explicit many-body interactions. The differences between our AIMD result and force-matched model result in higher coordination

Table 1. List of Nonbonding Parameters for the Force Field Developed in This Work^a

atoms	charge (e^-)	ϵ (kcal/mol)	σ (Å)
Li	1.0	0.10314	1.4424
P	1.07	0.13169	0.18489
F	−0.345	0.028716	2.9347
Li–Oc	NA	0.05551	2.398
Li–P	NA	0.014033	3.007
Li–O	NA	0.20937	2.0217
F–H	NA	0.2056	2.3951
F–CO	NA	0.06546	2.9381

^aThe geometric combination rule is used to generate the Lennard-Jones interactions, except for those explicitly listed in this table.

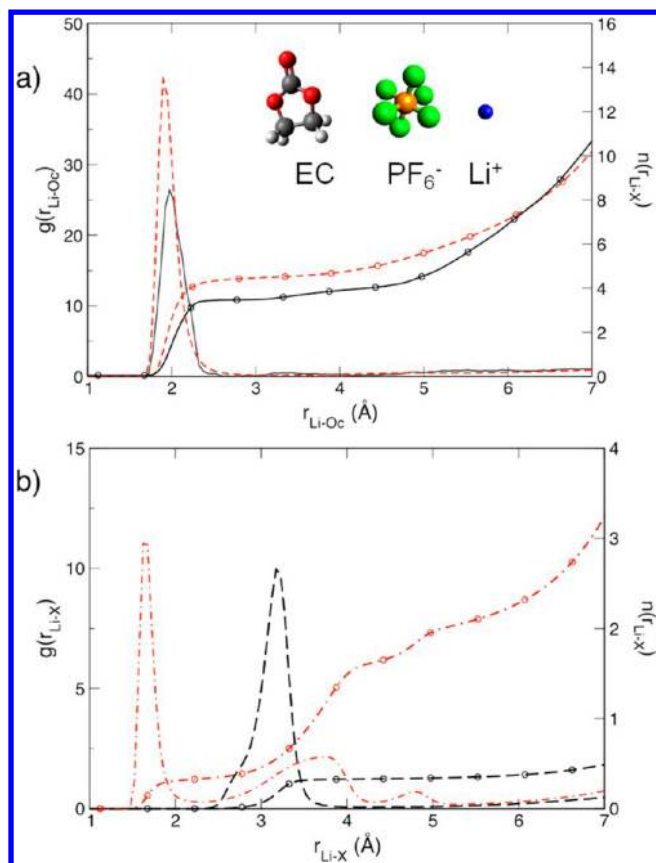


Figure 3. Comparison of the radial distribution function from the AIMD (black line) and force-matched model (red dashed line) for (a) Li–Oc, where Oc is a carbonyl oxygen from the EC solvent. The radial distributions for (b) Li–F (red dot-dashed line) and Li–P (black dashed line) from the force-matched model are also shown. The corresponding integrated coordination numbers are indicated by corresponding lines denoted with circles. Inset figures show the molecular structure of EC and LiPF_6 where atoms are color-coded for carbon (gray), oxygen (red), hydrogen (white), fluorine (green), phosphorus (orange), and lithium (blue).

numbers for the lithium ions, suggesting that our current version of the force field still over coordinates lithium; however, the agreement is much improved from previous nonpolarizable force fields. The Li–F and Li–P partial radial distribution functions are also shown in Figure 3b. The first peak in the Li–F radial distribution function (RDF) is due to the anions that

form part of the Li^+ solvation shell and hence the peak position is similar to that seen for Li–Oc. The peak in the Li–P distribution follows naturally from the location of the Li–F maximum and the fact that the fluorine will be located approximately a bond length away from the phosphorus to which it is bonded. In addition to accurate structural information, the Li^+ ion diffusion constant (determined from the slope of the curve of the mean square displacement with time) was found to be $2.0 \pm 0.5 \times 10^{-10} \text{ m}^2/\text{s}$, in excellent agreement with the work of Borodin et al. ($\sim 2 \times 10^{-10} \text{ m}^2/\text{s}$) using a polarizable model.⁷⁴

From our studies of the properties of the SEI materials in the bulk, it is evident that the two representative components selected for our SEI (lithium fluoride and dilithium ethylenedicarbonate) undergo phase separation when combined to form a solid. This phase separation of organic and inorganic species can be seen from the radial distribution functions discussed in the Supporting Information, and also verified by examining snapshots of the structure at the end of the equilibration phase, see Figure 4. With increasing LiF content, the two SEI components separate from each other and by 50% wt LiF adopt nearly layered structures. These findings could be important to understanding the formation of layered SEI materials in aged battery cells where kinetically favored distributions may differ, but over time a thermodynamically favored phase segregated system is observed. Such a separation of inorganic and organic species may also be driven by repeated dissolution of the Li_2EDC .^{20,51}

3.2. Simulations of the Electrochemical Cell. The Poisson potential across the cell for different applied voltages with the basal plane of the graphitic electrode and the edge plane electrodes are shown in Figure 1. The potential of zero charge (PZC) is determined from the change in the Poisson potential between the electrode and the central bulk-like electrolyte region of the cell at an applied voltage of 0 V. The PZC provides a qualitative measure of the affinity of the surface to various charged species,⁴⁶ and in both the basal (−0.17 V) and edge plane (−0.14 V) cases the PZC is negative. A negative value indicates that the positively charged Li^+ ions in the electrolyte have a lower propensity for the electrode surface than the negatively charged species; hence, one should expect that at these interfaces there is a relative reduction of Li^+ in comparison to the PF_6^- and EC oxygen groups. The PZC is slightly more negative for the basal plane compared to the edge plane which could indicate slightly greater affinity for Li^+ at the edge plane of graphite. These results are about a factor of 2

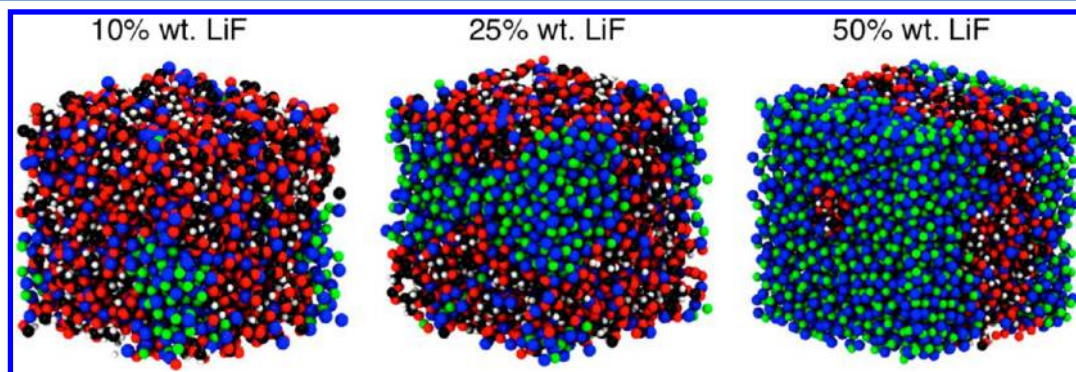


Figure 4. Equilibrated structures for the bulk SEI simulations with the indicated amounts of LiF present. In these snapshots, carbon atoms are shown in black, hydrogen in white, oxygen in red, lithium in blue, and fluorine in green.

smaller than the PZC reported by Vatamanu et al.;⁴⁶ however, in their simulations, significant amounts of DMC were also present at the interface and direct comparison is not possible.

The distribution of the various species in the electrolyte, that is, the EC, Li^+ , and PF_6^- in both basal and edge plane cells are shown in Figure 5 for the cases of 0 and 3 V applied potential.

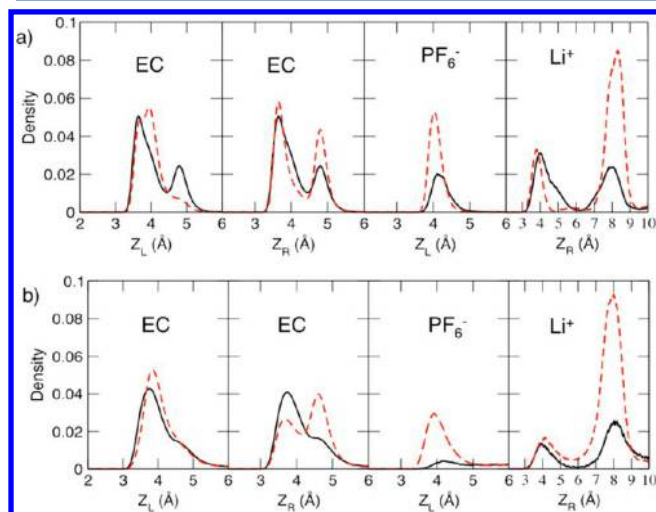


Figure 5. Normalized density distributions of electrolyte species at the (a) basal plane and (b) edge plane for 0 V (black lines) and 3 V (red dashed lines). In each panel, the species is indicated as well as which electrode in the simulation cell the distribution is measured from whether the left (Z_L) or the right (Z_R) side. The total numbers of each species differ in the two simulation cells and hence the densities have been normalized with respect to total number of particles.

The advantage of studying the whole cell in the simulation box is that one can probe both positive and negative voltage drops across the interfaces simultaneously with the change at either side of the simulation cell being roughly half the applied potential. Thus, at 3 V applied potential, we consider individual potential drops of about ± 1.5 V at either side of the system with respect to the bulk electrolyte region. The center of mass densities of the ethylene carbonate molecules at the two electrodes for the basal plane electrode and the edge plane case are compared in Figure 5. In both simulation cells, the agreement between the distributions at zero volts for the density at the left and right electrode interface of the simulation cell demonstrates that the electrolyte is well equilibrated as there is no bias on the system and symmetry is expected. In the case of zero applied bias voltage, one can also see clear differences in the structure of EC near the basal and edge planes.

Because the center of mass coordinate does not yield information on molecular orientation, the distribution in the angle formed by a fixed electrode plane, the ethylene carbonate center of mass, and its carbonyl oxygen at the negative electrode was considered in Figure 6 to provide greater insight into the double layer structure. The “electrode plane” is defined in this calculation as being parallel to the graphene sheets of the basal oriented electrode and perpendicular to the graphene sheets of the edge-oriented electrode. At the basal plane (black lines in Figure 6), the angular distributions show that EC exists primarily in configurations with the carbonyl group oriented parallel to the electrode plane (corresponding to $\alpha = 90^\circ$). At the edge planes, the EC is able to explore many more configurations in the absence of an applied field and the angular

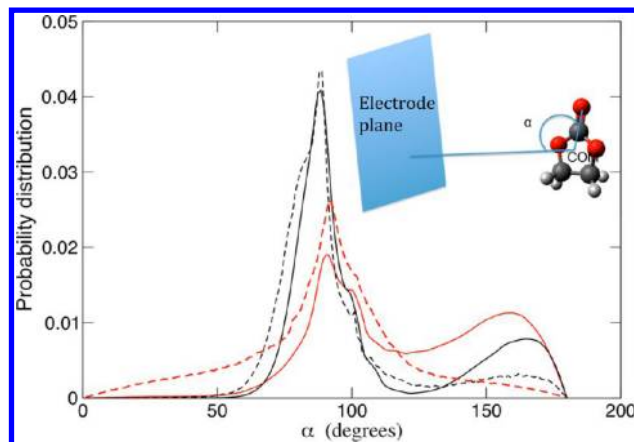


Figure 6. Probability distribution in the angle (α) formed at the negatively charged electrode by the electrode plane (defined parallel to the graphene sheets of the basal-oriented electrode and perpendicular to the graphene sheets of the edge-oriented electrode), the center of mass of the EC, and the carbonyl oxygen of EC, denoted Oc in the text. Distributions are shown for both the basal-oriented electrode (black lines) and the edge-oriented electrode (red lines) at 0 V (dashed lines) and 3 V (solid lines).

distribution is quite broad with a peak still centered at 90° , the value for configurations parallel to the electrode plane. However, with the application of an applied field, the range of geometries for EC are confined between two distinct limits: configurations in which its carbonyl group is oriented parallel to the electrode interface and a second class of configurations in which the carbonyl group is oriented perpendicular to the interface (see Figure 6). For the edge plane electrode, the first two peaks seen in Figure 5 are much broader than for the basal plane and the second peak appears only as a shoulder in the density, which agrees with the wider range of angles seen in Figure 6.

The application of an applied electric field modulates the ratios of these parallel and perpendicular configurations in a manner consistent with the partial charges on the molecule. The changes in peak heights with an applied field can be seen in Figure 5 and are attributed to increased probability of observing configurations with the carbonyl oxygen perpendicular to the electrode surface at the negative electrode to minimize repulsion between the surface negative charge and the carbonyl oxygen. In the case of the basal plane negative electrode, one sees two distinct peaks near 90° (parallel to electrode) and 180° (perpendicular with carbonyl group pointing away from the electrode). Very few solvent molecules show significant deviation from these two values, whereas for the edge plane case the distribution is once again wider and allows for other orientations between these values. At the positively charged electrode, shown in Figure 5, the EC density becomes more sharply peaked for both basal and edge plane at smaller electrode distances to allow for interaction between the carbonyl and ester oxygens with the positively charged electrode. Similar behavior was seen by Vatamanu et al. for EC electrolytes with a polarizable model and by Ohwaki et al. for propylene carbonate at a charged silicon surface using a DFT-based method.^{46,95}

While differing in the amount of ions present at their interfaces, the general behavior of the ion distributions with respect to applied fields at the basal and edge plane electrodes are quite similar. A clear general feature is that there are a

greater number of ions concentrated near the basal planes as opposed to the edge plane electrodes and this difference is attributed to the stronger ordering of the EC at the basal plane allowing for additive influence on the surrounding ions. However, for both the basal surface electrode and edge plane at 3 V, one can see in Figure 5 the distribution of PF_6^- ions is pulled closer to the positive electrode and its peak height increases substantially in magnitude at the interface, suggesting significant accumulation of negative ions. In both cases, the modification to the Li^+ density is minor within the surface layer at electrode interface, with a slight sharpening for the basal plane distribution and a negligible change in structure at the corresponding edge plane electrode. However, beyond the initial surface layer, there is a second peak in the Li^+ density, which displays the accumulation of positively charged ions with increased negative charge on the electrodes. This accumulation occurs beyond the surface layer as a result of the competition between the electrostatic interaction between Li^+ and the oriented EC molecules that are found pointing their negatively charged carbonyl group away from the electrode surface. Preferring to remain solvated, the Li^+ strongly favors being found outside of the surface layer of the electrode. From these density distributions, it is clear that the ethylene carbonate molecules form the first layer at both basal and edge plane electrode surfaces, but that PF_6^- also competes with EC to populate the region near the positive electrode. The distribution of the PF_6^- , based on the anions center of mass, at the left electrode (which is the positively charged electrode when a voltage is applied) shows a peak at around 4 Å. Given that the center of mass is approximately at the P atom and the P–F bond is around 1.6 Å, it is clear that these anions are also part of the first shell of electrolyte molecules near the electrode surface. The layers closest to the electrode are devoid of Li^+ , in agreement with the suspected strong coordination of lithium by EC and its reluctance to undergo desolvation.^{30,32}

As the voltage is increased above 3 V, the Li^+ cation distribution near the negative electrode surface of the basal plane remains fairly constant until one reaches 7 V, that is, 3.5 V across the negative electrode interface, at which point a peak suddenly emerges close to the electrode surface, at around 2.5 Å (see Figure 7). At this applied voltage, a few Li^+ ions form

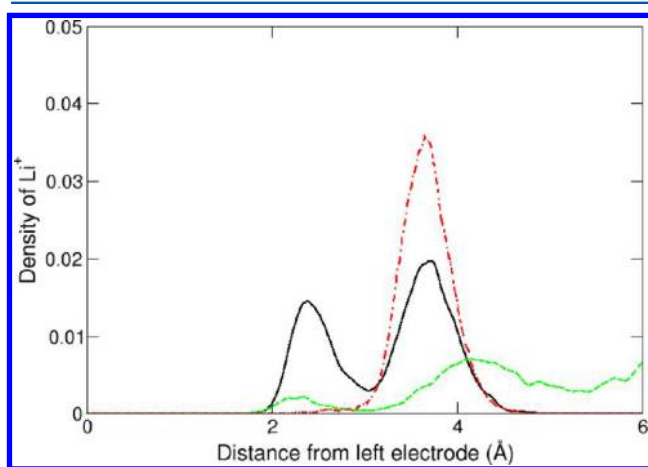


Figure 7. Density of lithium ions near the negative basal surface electrode at 4 V (red dot dashed line) and 7 V (black solid line) in addition to the density at the negative edge plane electrode at 4 V (green dashed line).

part of the first layer near the electrode and hence have undergone a significant distortion of their solvation shell. Interestingly, in the case of the edge plane, the Li^+ cation is seen to approach the electrode at a much smaller applied voltage of 4 V, corresponding to a 2 V potential drop across the negative electrode interface, as seen in Figure 7, and is attributed to the broader range of EC orientations at the edge plane interface, which more readily accommodate the extra Li ions.

To summarize the above observations, the edge plane electrodes allow for a greater amount of solvent disorder at the electrolyte interface as compared to the basal plane surface, and while this difference does not significantly impact the behavior of ion distributions at low applied voltages, at higher applied fields, the ability to draw Li^+ ions closer to the surface is greatly affected. These trends could be important to determining product formation during SEI growth, especially given the competition between the negative ions and the EC. Substantial crowding by PF_6^- could influence whether the one electron or two electron process dominates in EC reduction as a result of fewer ECs being available to interact with each other. The trends mentioned in the previous paragraphs regarding the structure of the electrolyte at the basal plane electrodes are in agreement with those obtained by Vatamanu et al. for the basal plane electrode/electrolyte interface using their polarizable electrolyte model and a few comments are warranted in comparing the two approaches.⁴⁶ In their work, they used the model of Reed and co-workers to model electrode polarization in which the polarization of the electrode is described by fluctuating Gaussian charge distributions at the electrode sites, with the value of these Gaussian charges determined at each step so as to maintain the electrode at a fixed potential (see ref 28b). This involves minimizing the total electrostatic energy at each step with respect to the electrode charges and in combination with their polarizable model creates an accurate, yet computationally expensive, approach. The method used in the present work is computationally simpler and yields the correct qualitative physics.

Having explored the general trends in electrolyte structure at a bare graphite electrode, we now consider the case where an SEI has begun to form and investigate its affect on electrolyte structure with the intent to gain insight into the impact on Li ion distributions as a function of SEI parameters. Representative equilibrated simulation cells are shown in Figure 8 with an applied potential of 0 V. As is obvious from the various Poisson potentials, the systems do not adopt symmetrical SEI films on either side of the simulation cell, but each side differs from its partner and these differences can create asymmetric potentials at the SEI-electrolyte interfaces even at zero applied bias voltage. Even so, a well-defined bulk electrolyte region is still recovered in which the potential is flat and can be used to define a PZC. As can be readily seen from these snapshots and is emphasized in Figures 9 and 10, the interface formed between the SEI and the electrolyte is not a simple flat surface as assumed for the bare electrode–electrolyte simulations. Rather the interface is highly structured with nonuniform SEI thickness that is especially pronounced for thin films, that is, thickness less than 1.0 nm. In the subsequent discussion, we shall find it convenient to refer to the SEI in the simulation based on its original uniform thickness at the beginning of the simulation, that is, 0.5–2.0 nm, but retain the understanding that these films are no longer uniform by the end of the simulation as they are allowed to interact with the electrode

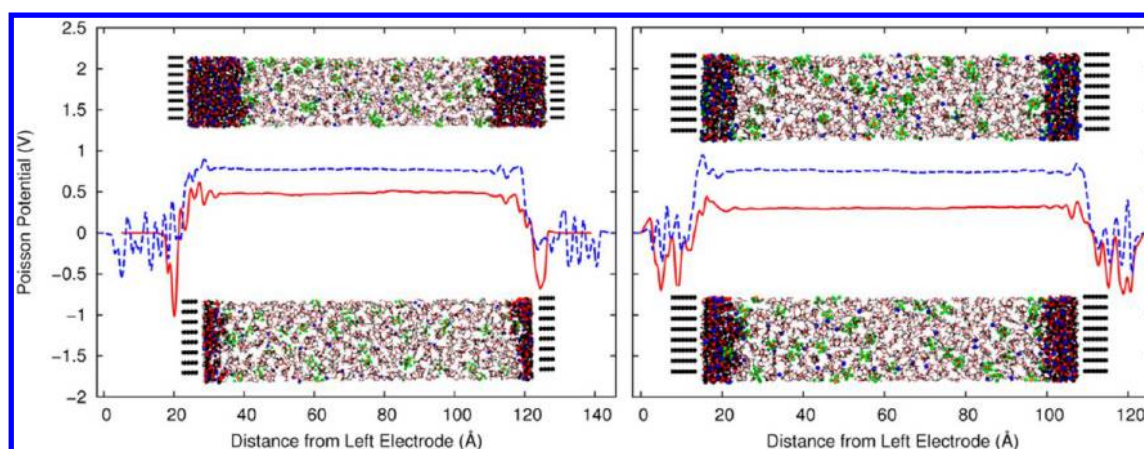


Figure 8. Example Poisson potentials for the electrochemical simulation cell with an SEI included at 0 V. In the left-hand panel, the results are shown for the SEI composed solely of Li_2EDC at a thickness of 0.5 nm (red solid line and lower inset) and 2.0 nm (blue dashed line and upper inset). The results for the smaller SEI have been shifted horizontally for graphing purposes. In the right-hand panel, results are shown for an SEI composed of only Li_2EDC 1.0 nm thick (red solid line and lower inset) in addition to an SEI of the same thickness composed of Li_2EDC and 25% by weight LiF (blue dashed lined and upper inset).

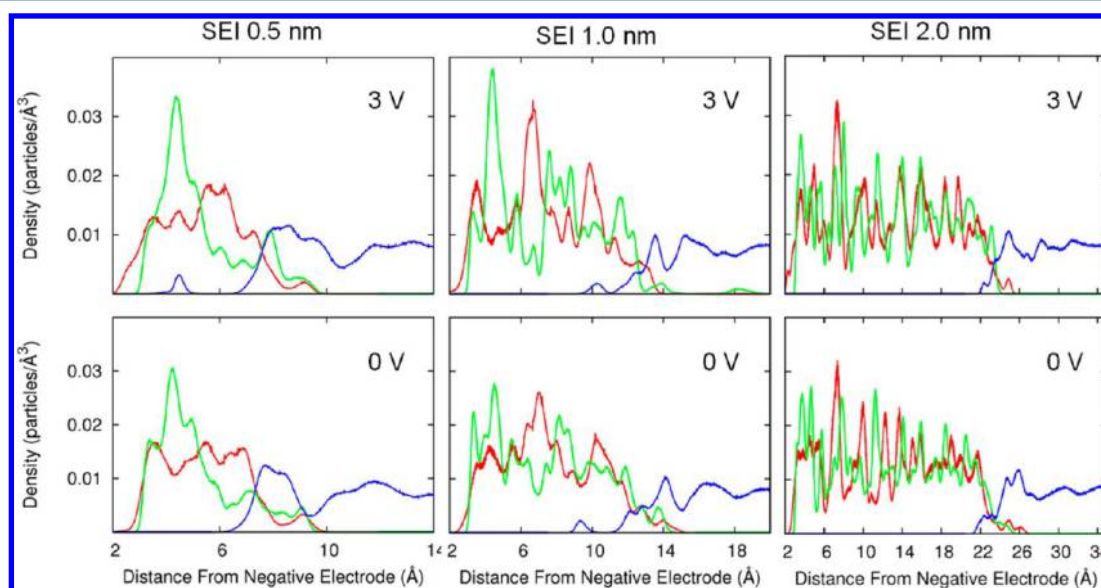


Figure 9. Density distributions for an electrochemical cell composed of an SEI of Li_2EDC and varying thickness. The thickness and voltages are indicated in each panel and the density of Li (red lines) and carbonate groups, by center of mass (green lines) in the SEI are shown along with the EC center of mass (blue lines).

charges and the electrolyte. Because we are mostly interested in Li^+ ion dynamics in this work, we will focus most of our attention on the right side SEI–electrolyte interface, also referred to as the negative electrode in our discussion.

From the PZC listed in Table 2, it is clear based on our qualitative discussion above that the SEI structures considered should be expected to not favor further lithium ion interactions. The most negative PZC arises from the 2.0 nm thick SEI with 0% LiF present, while the most positive PZC comes from the 1.0 nm thick SEI with 0% LiF . Interestingly this quantity does not show any clear trends with respect to the parameters of the SEI. With increasing SEI thickness and 0% LiF , one sees a substantial decrease from -0.14 V when no SEI is present to -0.48 V when a very thin SEI of 0.5 nm is added to the simulation cell. Upon further growth of the SEI layer to 1.0 nm however, the PZC becomes more positive before decreasing substantially again by 2.0 nm. The substantial drop by 2.0 nm could result qualitatively from effective screening of the

electrode polarization which prevents further attraction of ions from the solvent. With respect to changing the SEI composition, a very minimal decrease is seen between 10 wt % LiF and 50% wt LiF , while the middle value for 25% produces a clear uptick in PZC to -0.77 V. Based on these results, one would expect then that SEI thickness plays a much greater role in the ion distributions at the interfaces than the composition of the SEI itself, at least within our simple model consisting of only two SEI components. It should be emphasized that the PZC corresponds to the equilibrated interface between the SEI and the electrolyte which accounts for ion adsorption during the equilibration process. Hence, the distinction of which ions are favored at the interface is with respect to films that may already have several extra adsorbed ions from the electrolyte, as shown subsequently.

The complexity of the SEI–electrolyte interface is demonstrated in Figures 9 and 10 where the density distributions of the SEI components are shown along with the EC center of

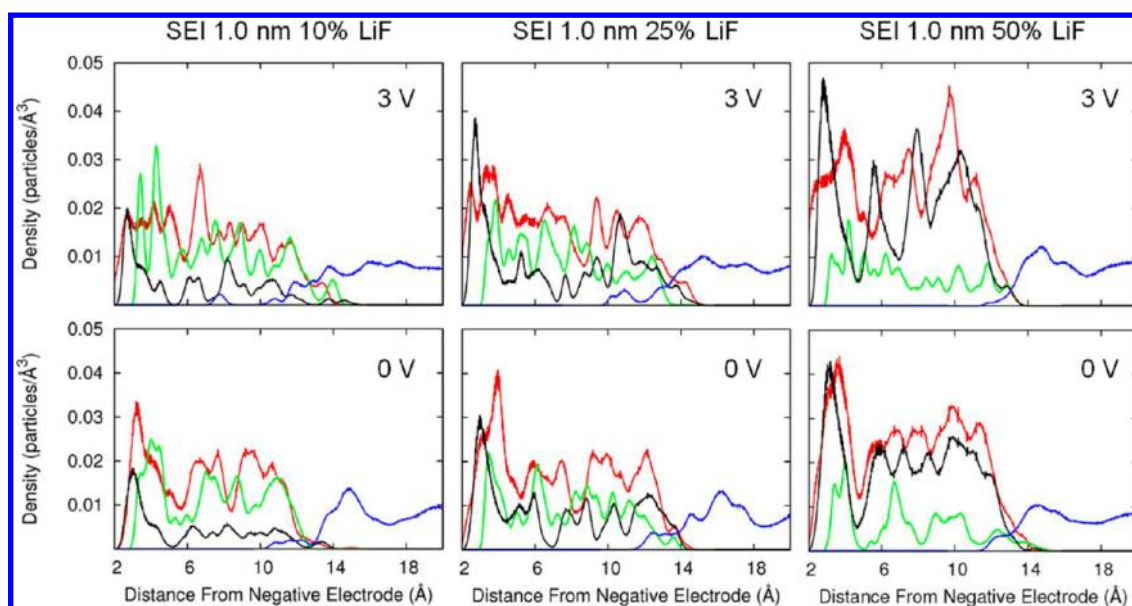


Figure 10. Density distributions for an electrochemical cell composed of an SEI of the same thickness, but varying composition by % weight of LiF. The composition and voltage are indicated in each panel and the density of Li (red lines), carbonate groups, by center of mass (green lines), and fluorine ions (black lines) in the SEI along with the EC center of mass (blue lines).

Table 2. Potentials of Zero Charge (PZC) for Simulation Cells with an SEI Attached to the Graphite Electrodes and the Estimated Potential Drop within the SEI at an Applied Bias of 3 V

thickness (nm)	% LiF	PZC (V)	internal potential drop (V)
0.5	0	−0.48	NA
1.0	0	−0.30	0.9
1.0	10	−0.67	1.0
1.0	25	−0.77	1.1
1.0	50	−0.70	1.2
2.0	0	−0.78	1.0

mass density profile. One can see that in all instances with zero applied volts, the EC density and SEI density overlap in a region varying from 2 to 5 Å in width at the interface between these materials. Inspection of MD snapshots reveals that these regions do not involve direct insertion of the EC into the SEI, but rather represents deformation of the SEI surface to allow for intrusion of EC from the electrolyte, which remains in contact with other species from the electrolyte. Hence, these intrusions do not represent stripping the solvent entirely from a molecule to allow it to diffuse within the SEI layer. Furthermore, the observed reduction of EC penetration into the SEI layer with increasing SEI thickness implies that film deformation is associated with the cohesiveness of the SEI film. For smaller film thickness, the interactions between the electrolyte and electrode are less screened and the SEI is prone to be deformed into a porous structure to provide increased interactions between the electrode and electrolyte. As the film grows, the cost for such deformation increases and hence is not observed as prevalently. Regarding changes to the composition of the SEI, addition of LiF also seems to favor a sharper interface with EC. This could be explained by a net unfavorable interaction between the highly ionic LiF and the smaller partial charges of EC in addition to a cohesion argument based on not wanting to break up LiF groups. In all cases, it should also be noted that the effect of the SEI is to

significantly reduce the structuring of EC seen for the bare electrode surfaces. The center of mass profiles for EC show only minor structure as one approaches the interface, implying that there is no predominant orientation, and the EC quickly attains a bulk density value a nanometer away from the interface. These results are in contrast to those for the bare electrode in which the EC structuring resulted in factors of 4 changes in center of mass densities near the interfaces.

Regarding the SEI films themselves, a surprising agreement is seen between Figures 9 and 10 and the expectations from the proposed layer model for the SEI when organic and inorganic components are present. As mentioned earlier, it has been posited that the SEI consists of a compact inorganic phase in addition to a porous organic layer. While the formation of a porous organic network was not seen in our very thin SEI films, given the above discussion of the ability for the EC electrolyte to mix with the SEI outer layer lends plausibility to the formation of structures closely associating EC with Li₂EDC during repeated dissolution/deposition upon charge cycling. More quantitatively, one can clearly see in the zero volts case for the SEI simulations containing LiF, the development of concentrated regions of fluorine within the first 4 Å of the SEI, in agreement with the qualitative description of a layered model. While complete phase segregation of the scale seen in Figure 4 was not observed, one can clearly see a propensity for the inorganic salt to collect at the graphite electrode interface, in agreement with experimental observations. At the highest LiF content, the trend is present, as well as a series of anticorrelated peaks between the Li and F, as expected for the formation of a more ordered solid.

A final interesting aspect of the SEI structure is its behavior with respect to bias voltage. It is clear from Figures 9 and 10 that applying a potential to the system results in significant polarization of the SEI itself by rearrangement of its components. With regards to thickness of the SEI, it appears that the effect is greatly dampened in going from 1.0 to 2.0 nm, where the density distributions do not change in the same readily identified manner seen for the 0.5 and 1.0 nm thick

films. The changes in EC distributions when a bias voltage is introduced are also more subtle than seen in the bare electrode simulations. In several cases, the EC distribution hardly changes aside from a reduction of EC overlap with the SEI layer region. The exception to this trend is for the smallest SEI layer studied, in which case the changes in the layer allow for EC to come into contact with the underlying electrode surface. The lack of substantial changes to the EC density profiles with applied field as opposed to the SEI rearrangements implies that the SEI layer effectively screens the electrolyte from the electric field. To provide a slightly more quantitative view of this behavior, the Poisson potential was considered 6 Å into the SEI region from the electrode surface for the 1.0 and 2.0 nm SEI films. The Poisson potential in all five instances was found to oscillate around an average value within the first 6–10 Å and the average is reported in Table 2 with respect to the negative electrode potential. While this number does not change substantially as the SEI thickness and composition changes, it is clear that a substantial portion of the voltage drop has already occurred in these systems as the interface region is approached. In all five cases, the applied bias was 3 V, which means that roughly 50% of the potential drop across each interface comes from the SEI itself. The averaging procedure could not be carried out for the 0.5 nm SEI because it is too intimately mixed with the electrolyte to distinguish a strictly SEI contribution. Probing the internal potentials of these SEI materials provides a promising future bridge to informing full cell engineering models, which often rely on solving for the potential drop across the SEI.

Having discussed the properties of the EC and SEI materials under applied fields, we now consider the behavior of the ions in the system. Figure 11 shows a representative result for the ion densities at the SEI–electrolyte region and demonstrates a clear distinction between two different regimes of ion interaction. In both the lithium and PF_6^- density profiles, one clearly sees the presence of density inside the SEI region

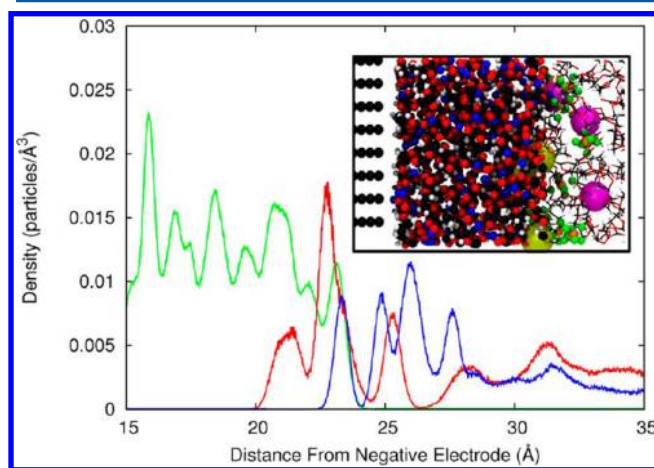


Figure 11. Representative density distributions at the SEI–electrolyte interface with an SEI consisting of Li_2EDC 2.0 nm thick at an applied potential of 3 V. Densities for lithium in the SEI (green line), lithium ions from the electrolyte (red line), and the center of mass for the PF_6^- ions (blue line) are shown. The distributions for the electrolyte species have been scaled by a factor of 4 for graphing purposes. The inset shows the physical location of two different regions of lithium ions from the electrolyte, enlarged yellow spheres are lithium ions less than 24 Å from the electrode surface and enlarged magenta spheres are lithium ions between 24 and 32 Å from the electrode surface.

and, as mentioned earlier for the case of EC, these distributions do not represent complete insertion into the SEI material. However, the presence of ions so closely associated with the SEI interface does imply that they have lost some of their solvation shell and are adsorbed to the SEI surface. This description is verified by the inset snapshot, which highlights two regions at the SEI–electrolyte interface. Lithium ions from the electrolyte that are less than 24 Å away from the electrode surface are highlighted as enlarged yellow spheres, while lithium ions from the electrolyte which are between 24 and 32 Å from the electrode are highlighted as enlarged magenta spheres. Clearly the ions adsorbed at the SEI surface have lost their original solvation structure, while the ions located in the farther region from the electrode retain EC and PF_6^- in their solvation shell. This natural division between types of ions, namely, those found within the SEI region in the density distribution and those outside of the SEI density region, can be used to define boundaries for integrating the ion densities to yield the amounts of adsorbed species and accumulation of ions near the SEI surfaces.

Figure 12 shows the total accumulated ion densities at the SEI–electrolyte interface as a function of SEI thickness and

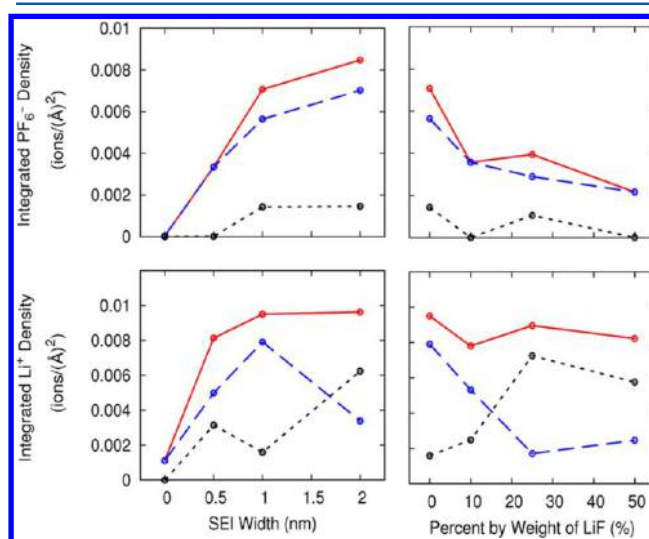


Figure 12. Integrated ion densities at the SEI–electrolyte interface as a function of SEI thickness and composition, as indicated. The total accumulated density up to 6 Å into the electrolyte region is shown for the lithium and PF_6^- ions (red solid lines), as well as the division of the density into an ion-adsorbed region (black dotted lines) and 6 Å from this region into the bulk electrolyte region near the interface (blue dashed lines). For determination of the adsorbed region, see discussion in the text.

composition, as indicated. It is of interest to note that the total accumulation of lithium ions at the 1.0 nm SEI's with varying amounts of LiF did not change markedly as a function of fluoride content, which would seem to agree with the previous observation from the PZC's that these interfaces do not differ greatly in their general attraction for lithium ions. The consistency in the total accumulated density is supported by counter trends in the lithium distribution with lithium being more likely to be adsorbed to the higher LiF content SEI's at the expense of depleting the nearby electrolyte region. This implies that with increasing LiF content, lithium ions from the electrolyte are drawn closer to the surface. In the case of PF_6^- ions, few are seen being drawn in as far as the lithium ions

which is to be expected given the much bulkier size of the anion. As a result, the PF_6^- is relegated to the electrolyte region neighboring the SEI surface. Furthermore, fewer anions are found close to the interface in general as the amount of LiF increases, suggesting that the anions do not interact favorably with the fluoride and that qualitatively different ion distributions are found in the electrolyte regions near purely Li_2EDC SEIs and those containing LiF. This trend is supported by the graphs of integrated density with respect to changes in SEI thickness. For surface films composed solely of Li_2EDC , one sees a clear propensity to attract more Li^+ and PF_6^- with increasing film thickness. In going from 0.5 to 2.0 nm, one also sees an increase in the amount of adsorbed lithium, indicating that, as in the case of increasing LiF content, increasing thickness seems to draw lithium ions from the electrolyte close to the SEI structure.

To briefly summarize these results, the presence of the SEI plays the role of screening the electric field and, hence, reducing the restructuring of the solvent under the applied field. The structures of the SEI seen in this work seem to agree with the layered model proposed by several previous authors in which organic and inorganic components tend to separate in these surface films. The amorphous nature of the SEI also seems to prohibit structuring of the EC as seen in the bare surface cases. With increasing thickness and increasing amounts of LiF, more lithium ions are seen to adsorb to the SEI surface and it is assumed that greater amounts of adsorption could translate to more readily allowing for lithium ion desolvation, a process identified as important to the operation of rechargeable batteries. The fact that partial desolvation is seen in our simulations implies that the interpretation of IES experiments may be more complicated than originally thought because desolvation may not be as slow, but perhaps actual insertion into the SEI and diffusion are rate determining steps. While neither process was observed in these simulations, they were probably precluded from the outset by not allowing for lithium intercalation into the graphite particle, which could then provide the vacancy for addition of lithium ions from the electrolyte.

4. CONCLUSIONS

A computationally efficient method has been presented to study for the first time the structure of the electrode–SEI–electrolyte interface from an atomistic perspective. Information from experiment was used to construct the simulation cells and encouraging agreement was found with previous work on bare graphite electrode surfaces and bulk electrolyte systems. Density distributions for ethylene carbonate and the ionic species were used to understand the structure of the SEI–electrolyte interface and to study the effects of SEI thickness and composition on the electrolyte. The application of electric fields revealed under applied fields revealed substantial polarization of the SEI and significant effects on local ion adsorption. These efforts represent the first attempt to use computational modeling to address the question of how properties of the SEI effect the electrolyte. While this paper has been focused on structural aspects, future work naturally needs to be done to extract free energy barriers to lithium insertion and diffusion within the SEI. This work has also demonstrated the utility of force-matching to develop electrolyte force fields and provide an improved pairwise model which captures more of the essential physics without being too computationally cumbersome.

■ ASSOCIATED CONTENT

Supporting Information

The simulation details for the studies performed on bulk solid electrolyte interphase materials, i.e., in the absence of the graphite interface and the electrolyte, along with further information on the reported densities and radial distribution functions are provided. This material is available free of charge via the Internet at <http://pubs.acs.org>.

■ AUTHOR INFORMATION

Corresponding Author

*E-mail: gavoth@uchicago.edu.

Author Contributions

[†]These authors contributed equally.

Notes

The authors declare no competing financial interest.

■ ACKNOWLEDGMENTS

Support from the U.S. Department of Energy's Vehicle Technologies Program, specifically from Tien Duong, is gratefully acknowledged. This research was also supported by the University of Chicago and the Department of Energy under Department of Energy Contract No. DE-AC02-06CH11357 awarded to UChicago Argonne, LLC, operator of Argonne National Laboratory.

■ REFERENCES

- (1) Winter, M.; Brodd, R. J. *Chem. Rev.* **2004**, *2004*, 4245–4269.
- (2) Thackeray, M. M.; Wolverton, C.; Isaacs, E. D. *Energy Environ. Sci.* **2012**, *5*, 7854–7863.
- (3) Solomon, S.; Qin, D.; Manning, M.; Chen, Z.; Marquis, M.; Averyt, K. B.; Tignor, M.; Miller, H. L., Eds. *Working Group I to the Fourth Assessment Report of the Intergovernmental Panel on Climate Change*, 2007; Cambridge University Press: New York, 2007.
- (4) *Annual Energy Review 2009*; U.S. Energy Information Administration: Washington, DC, 2010.
- (5) Etacheri, V.; Marom, R.; Elazari, R.; Salitra, G.; Aurbach, D. *Energy Environ. Sci.* **2011**, *4*, 3243–3262.
- (6) Xu, K.; von Cresce, A. J. *Mater. Chem.* **2011**, *21*, 9849–9864.
- (7) Verma, P.; Maire, P.; Novák, P. *Electrochim. Acta* **2010**, *55*, 6332–6341.
- (8) Winter, M. Z. *Phys. Chem.* **2009**, *223*, 1395–1406.
- (9) Peled, E. J. *Electrochem. Soc.* **1979**, *126*, 2047–2051.
- (10) Aurbach, D. J. *Power Sources* **2000**, *89*, 206–218.
- (11) Smith, A. J.; Burns, J. C.; Zhao, X.; Xiong, D.; Dahn, J. R. J. *Electrochem. Soc.* **2011**, *158*, A447–A452.
- (12) Andersson, A. M.; Henningson, A.; Siegbahn, H.; Jansson, U.; Edström, K. J. *Power Sources* **2003**, *119–121*, 522–527.
- (13) Peled, E.; Bar Tow, D.; Merson, A.; Gladkikh, A.; Burstein, L.; Golodnitsky, D. J. *Power Sources* **2001**, *97–98*, 52–57.
- (14) Dedryvère, R.; Leroy, S.; Martinez, H.; Blanchard, F.; Lemordant, D.; Gonbeau, D. J. *Phys. Chem. B* **2006**, *110*, 12986–12992.
- (15) Tang, M.; Miyazaki, K.; Abe, T.; Newman, J. J. *Electrochem. Soc.* **2012**, *159*, A634–A641.
- (16) Herstedt, M.; Andersson, A. M.; Rensmo, H.; Siegbahn, H.; Edström, K. *Electrochim. Acta* **2004**, *49*, 4939–4947.
- (17) Spahr, M. E.; Goers, D.; Märkle, W.; Dentzer, J.; Würsig, A.; Buga, H.; Vix-Guterl, C.; Novák, P. *Electrochim. Acta* **2010**, *55*, 8928–8937.
- (18) Peled, E.; Golodnitsky, D.; Ulus, A.; Yufit, V. *Electrochim. Acta* **2004**, *50*, 391–395.
- (19) Haik, O.; Ganin, S.; Gershinsky, G.; Zinigrad, E.; Markovsky, B.; Aurbach, D.; Halalay, I. J. *Electrochem. Soc.* **2011**, *158*, A913–A923.

- (20) Bridges, C. A.; Sun, X.-G.; Zhao, J.; Paranthaman, M. P.; Dai, S. *J. Phys. Chem. C* **2012**, *116*, 7701–7711.
- (21) Kang, S.-H.; Abraham, D. P.; Xiao, A.; Lucht, B. L. *J. Power Sources* **2008**, *175*, 526–532.
- (22) Zhuang, G. V.; Xu, K.; Yang, H.; Jow, T. R.; Ross, P. N. *J. Phys. Chem. B* **2005**, *109*, 17567–17573.
- (23) Lu, P.; Harris, S. J. *Electrochem. Commun.* **2011**, *13*, 1035–1037.
- (24) Mukherjee, P.; Lagutchev, A.; Dlott, D. D. *J. Electrochem. Soc.* **2012**, *159*, A244–A252.
- (25) Xu, K.; Lam, Y.; Zhang, S.; Jow, T. R.; Curtis, T. B. *J. Phys. Chem. C* **2007**, *111*, 7411–7421.
- (26) Xu, K. *Chem. Rev.* **2004**, *104*, 4303–4417.
- (27) Märkle, W.; Lu, C.-Y.; Novák, P. *J. Electrochem. Soc.* **2011**, *158*, A1478–A1482.
- (28) Nakagawa, H.; Domi, Y.; Doi, T.; Ochida, M.; Tsubouchi, S.; Yamanaka, T.; Abe, T.; Ogumi, Z. *J. Power Sources* **2012**, *206*, 320–324.
- (29) Wang, L.; Deng, X.; Dai, P.-X.; Guo, Y.-G.; Wang, D.; Wan, L.-J. *Phys. Chem. Chem. Phys.* **2012**, *14*, 7330–7336.
- (30) Xu, K.; Von Cresce, A.; Lee, U. *Langmuir* **2010**, *26*, 11538–11543.
- (31) Xu, K. *J. Electrochem. Soc.* **2007**, *154*, A162–A167.
- (32) Abe, T.; Fukuda, H.; Iriyama, Y.; Ogumi, Z. *J. Electrochem. Soc.* **2004**, *151*, A1120–A1123.
- (33) Jow, T. R.; Marx, M. B.; Allen, J. L. *J. Electrochem. Soc.* **2012**, *159*, A604–A612.
- (34) Computational Materials Science and Chemistry for Innovation, Bethesda, MD, July 26–28, 2010, Department of Energy: Washington, DC, 2010.
- (35) Wang, Y.; Nakamura, S.; Ue, M.; Balbuena, P. B. *J. Am. Chem. Soc.* **2001**, *123*, 11708–11718.
- (36) Vollmer, J. M.; Curtiss, L. A.; Vissers, D. R.; Amine, K. *J. Electrochem. Soc.* **2004**, *151*, A178–A183.
- (37) Tasaki, K. *J. Phys. Chem. B* **2005**, *109*, 2920–2933.
- (38) Xing, L.; Li, W.; Wang, C.; Gu, F.; Xu, M.; Tan, C.; Yi, J. *J. Phys. Chem. B* **2009**, *113*, 16596–16602.
- (39) Xing, L.; Wang, C.; Li, W.; Xu, M.; Meng, X.; Zhao, S. *J. Phys. Chem. B* **2009**, *113*, 5181–5187.
- (40) Xing, L.; Borodin, O. *Phys. Chem. Chem. Phys.* **2012**, *14*, 12838–12843.
- (41) Yu, J.; Balbuena, P. B.; Budzien, J.; Leung, K. *J. Electrochem. Soc.* **2011**, *158*, A400–A410.
- (42) Xing, L.; Borodin, O.; Smith, G. D.; Li, W. *J. Phys. Chem. A* **2011**, *115*, 13896–13905.
- (43) Bedrov, D.; Smith, G. D.; van Duin, A. C. T. *J. Phys. Chem. A* **2012**, *116*, 2978–2985.
- (44) Márquez, A.; Balbuena, P. B. *J. Electrochem. Soc.* **2001**, *148*, A624–A635.
- (45) Smith, G. D.; Borodin, O.; Russo, S. P.; Rees, R. J.; Hollenkamp, A. F. *Phys. Chem. Chem. Phys.* **2009**, *11*, 9884–9897.
- (46) Vatamanu, J.; Borodin, O.; Smith, G. D. *J. Phys. Chem. C* **2011**, *116*, 1114–1121.
- (47) Xing, L.; vatamanu, J.; Smith, G. D.; Bedrov, D. *J. Phys. Chem. Lett.* **2012**, *3*, 1124–1129.
- (48) Hamad, I. A.; Novotny, M. A.; Wipf, D. O.; Rikvold, P. A. *Phys. Chem. Chem. Phys.* **2009**, *12*, 2740–2743.
- (49) Wang, Y.; Balbuena, P. B. *J. Phys. Chem. B* **2003**, *107*, 5503–5510.
- (50) Tasaki, K.; Goldberg, A.; Winter, M. *Electrochim. Acta* **2011**, *56*, 10424–10435.
- (51) Tasaki, K.; Harris, S. J. *J. Phys. Chem. C* **2010**, *114*, 8076–8083.
- (52) Leung, K. *J. Phys. Chem. C* **2012**, *116*, 9852–9861.
- (53) Leung, K.; Budzien, J. *Phys. Chem. Chem. Phys.* **2010**, *12*, 6583–6586.
- (54) Kim, S.-P.; van Duin, A. C. T.; Shenoy, V. B. *J. Power Sources* **2011**, *196*, 8590–8597.
- (55) Chen, Y. C.; Ouyang, C. Y.; Song, L. J.; Sun, Z. L. *J. Phys. Chem. C* **2011**, *115*, 7044–7049.
- (56) Iddir, H.; Curtiss, L. A. *J. Phys. Chem. C* **2010**, *114*, 20903–20906.
- (57) Borodin, O.; Smith, G. D.; Fan, P. *J. Phys. Chem. B* **2006**, *110*, 22773–22779.
- (58) Srinivasan, V.; Newman, J. *J. Electrochem. Soc.* **2004**, *151*, A1530–A1538.
- (59) Subramanian, V. R.; Boovaragavan, V.; Diwakar, V. D. *Electrochem. Solid-State Lett.* **2007**, *10*, A255–A260.
- (60) Kumaresan, K.; Sikha, G.; White, R. E. *J. Electrochem. Soc.* **2008**, *155*, A164–A171.
- (61) Wang, C.-W.; Sastry, A. M. *J. Electrochem. Soc.* **2007**, *154*, A1035–A1047.
- (62) Safari, M.; Delacourt, C. *J. Electrochem. Soc.* **2011**, *158*, A562–A571.
- (63) Kim, G.-H.; Smith, K.; Lee, K.-J.; Santhanagopalan, S.; Pesaran, A. *J. Electrochem. Soc.* **2011**, *158*, A955–A969.
- (64) Zadin, V.; Brandell, D.; Kasemägi, H.; Aabloo, A.; Thomas, J. O. *Solid State Ionics* **2010**, *192*, 279–283.
- (65) Christensen, J.; Newman, J. *J. Electrochem. Soc.* **2004**, *151*, A1977–A1988.
- (66) Sankarasubramanian, S.; Krishnamurthy, B. *Electrochim. Acta* **2012**, *70*, 248–254.
- (67) Ramadass, P.; Haran, B.; Gomadam, P. M.; White, R.; Popov, B. N. *J. Electrochem. Soc.* **2004**, *151*, A196–A203.
- (68) Ganesh, P.; Jiang, D.; Kent, P. R. C. *J. Phys. Chem. B* **2011**, *115*, 3085–3090.
- (69) Postupna, O. O.; Kolesnik, Y. V.; Kalugin, O. N.; Prezhdo, O. V. *J. Phys. Chem. B* **2011**, *115*, 14563–14571.
- (70) Soetens, J.-C.; Millot, C.; Maigret, B. *J. Phys. Chem. A* **1998**, *102*, 1055–1061.
- (71) Li, T.; Balbuena, P. B. *J. Electrochem. Soc.* **1999**, *146*, 3613–3622.
- (72) Masia, M.; Probst, M.; Rey, R. *J. Phys. Chem. B* **2004**, *108*, 2016–2027.
- (73) Tasaki, K.; Kanda, K.; Nakamura, S.; Ue, M. *J. Electrochem. Soc.* **2003**, *150*, A1628–A1636.
- (74) Borodin, O.; Smith, G. D. *J. Phys. Chem. B* **2009**, *113*, 1763–1776.
- (75) Sun, H. *J. Phys. Chem. B* **1998**, *102*, 7338–7364.
- (76) Maple, J. R.; Hwang, M.-J.; Stockfisch, T. P.; Dinur, U.; Waldman, M.; Ewig, C. S.; Hagler, A. T. *J. Comput. Chem.* **1994**, *15*, 162–182.
- (77) Sun, H.; Mumby, S. J.; Maple, J. R.; Hagler, A. T. *J. Am. Chem. Soc.* **1994**, *116*, 2978–2987.
- (78) Izvekov, S.; Voth, G. A. *J. Chem. Phys.* **2005**, *123*, 134105.
- (79) Izvekov, S.; Voth, G. A. *J. Phys. Chem. B* **2005**, *109*, 2469–2473.
- (80) Knight, C.; Voth, G. A. *Mol. Phys.* **2012**, *110*, 935–944.
- (81) Carlson, H. A.; Nguyen, T. B.; Orozco, M.; Jorgensen, W. L. *J. Comput. Chem.* **1993**, *14*, 1240–1249.
- (82) Noid, W. G.; Chu, J.-W.; Ayton, G. S.; Krishna, V.; Izvekov, S.; Voth, G. A.; Das, A.; Andersen, H. C. *J. Chem. Phys.* **2008**, *128*, 244114.
- (83) Noid, W. G.; Liu, P.; Wang, Y.; Chu, J.-W.; Ayton, G. S.; Izvekov, S.; Andersen, H. C.; Voth, G. A. *J. Chem. Phys.* **2008**, *128*, 244115.
- (84) Singh, U. C.; Kollman, P. A. *J. Comput. Chem.* **1984**, *5*, 129–145.
- (85) Mundy, C. J.; Del Ben, M.; Schiffman, F.; Forbert, H.; Bethune, I.; Hutter, J.; Walewski, L.; Iannuzzi, M.; Krack, M.; Ribeiro, C. P.; et al. CP2K, 2012.
- (86) CP2K Homepage, <http://www.cp2k.org>, 2012.
- (87) Plimpton, S. J. *J. Comput. Phys.* **1995**, *117*, 1–9.
- (88) LAMMPS Homepage, <http://lammps.sandia.gov>, 2012.
- (89) Frisch, M. J.; Trucks, G. W.; Schlegel, H. B.; Scuseria, G. E.; Robb, M. A.; Cheeseman, J. R.; Scalmani, G.; Barone, V.; Mennucci, B.; Petersson, G. A.; et al. *Gaussian 09*; Gaussian Inc.: Wallingford, CT, 2009.
- (90) Peng, Z.; Ewig, C. S.; Hwang, M.-J.; Waldman, M.; Hagler, A. T. *J. Phys. Chem. A* **1997**, *101*, 7243–7252.

- (91) Petersen, M. K.; Kumar, R.; White, H. S.; Voth, G. A. *J. Phys. Chem. C* **2012**, *116*, 4903–4912.
- (92) Luque, N. B.; Schmickler, W. *Electrochim. Acta* **2012**, *71*, 82–85.
- (93) Ganesh, P.; Jiang, D. E.; Kent, P. R. C. *J. Phys. Chem. B* **2011**, *115*, 3085–3090.
- (94) Kameda, Y.; Umebayashi, Y.; Takeuchi, M.; Wahab, M. A.; Fukuda, S.; Ishiguro, S. I.; Sasaki, M.; Amo, Y.; Usuki, T. *J. Phys. Chem. B* **2007**, *111*, 6104–6109.
- (95) Ohwaki, T.; Otani, M.; Ikeshoji, T.; Ozaki, T. *J. Chem. Phys.* **2012**, *136*, 134101.